DEVELOPMENT OF ELECTRON BERNSTEIN WAVE RESEARCH IN MAST

V. SHEVCHENKO,[a]* G. CUNNINGHAM,[a] A. GURCHENKO,[b] E. GUSAKOV,[b] B. LLOYD,[a]
M. O'BRIEN,[a] A. SAVELIEV,[b] A. SURKOV,[b] F. VOLPE,[a] and M. WALSH[a]

[a]*EURATOM/UKAEA Fusion Association, Culham Science Centre, Abingdon, Oxon OX14 3DB, United Kingdom*
[b]*Ioffe Institute, Politekhnicheskaya 26, 194021 St. Petersburg, Russia*

Received September 15, 2006
Accepted for Publication January 10, 2007

Burning plasma spherical tokamaks (STs) rely on off-axis current drive (CD) and nonsolenoid start-up techniques. Electron Bernstein waves (EBWs) may provide efficient off-axis heating and CD in high-density ST plasmas. EBWs may also be used in the plasma start-up phase because EBW absorption and CD efficiency remain high even in relatively cold plasmas. EBW studies on the Mega Ampere Spherical Tokamak (MAST) can be subdivided into four separate subjects: thermal electron cyclotron emission observations from overdense plasmas, EBW modeling, proof-of-principle EBW heating experiments with the existing 60-GHz gyrotrons, and EBW assisted plasma start-up at 28 GHz. These studies are also aimed at determining the potential for a high-power EBW system for heating and CD in MAST. The optimum choice of frequency and launch configuration is a key issue for future applications in MAST. This paper describes diagnostics, modeling tools, and high-power radio frequency systems developed specifically for EBW research in MAST. The experimental methodology employed in proof-of-principle EBW heating experiments along with experimental results is discussed in detail. EBW heating via the ordinary-extraordinary-Bernstein (O-X-B) mode conversion has clearly been observed for the first time in an ST.

KEYWORDS: *electron Bernstein wave, electron cyclotron resonance heating, spherical tokamak*

Note: Some figures in this paper are in color only in the electronic version.

I. INTRODUCTION

The Mega Ampere Spherical Tokamak (MAST) program is focused on exploring the potential of the spherical tokamak (ST) concept as a basis of a fusion component test facility and a high-beta fusion power plant. Burning plasma STs rely on off-axis current drive (CD) and nonsolenoid start-up techniques. Electron Bernstein waves (EBWs) may provide efficient off-axis heating and CD in high-density ST plasmas. It has been predicted theoretically[1] and confirmed experimentally[2,3] that the EBW CD efficiency exceeds that achievable with conventional electron cyclotron (EC) resonance heating (ECRH) for similar plasma parameters.[4,5] In COMPASS-D experiments, extraordinary-Bernstein (X-B) mode conversion (MC) with the extraordinary (X)-mode launched from the high field side (HFS) has been exploited.[2] The achieved EBW CD efficiency was $\eta_{20\mathrm{CD}} \sim 0.035\ \mathrm{AW}^{-1}\,\mathrm{m}^{-2}$. The value $\eta_{20\mathrm{CD}}$ is defined as $n_{e20} I_{\mathrm{CD}} R P_{\mathrm{RF}}^{-1}$, where n_{e20} is a line-averaged density in $10^{20}\,\mathrm{m}^{-3}$, I_{CD} is the radio-frequency (RF)–driven current in A, R is the major radius in m, and P_{RF} is the absorbed RF power in W. Following successful demonstration of EBW CD on COMPASS-D, EBW experiments have continued in MAST using the existing 60-GHz, 1-MW complex.

Conventional ECRH and CD methods typically cannot be used in STs because of the specific plasma parameters. Usually the plasma is well overdense in STs, i.e., $\omega_{pe} \gg \omega_{ce}$, where ω_{pe} and ω_{ce} are the electron plasma and EC frequencies, respectively. In such plasmas the core is inaccessible for conventional electromagnetic modes in the range of frequencies corresponding to the first few EC harmonics. This is primarily because EC resonances in the core plasma are completely obscured by the ordinary (O)-mode and X-mode cutoffs as illustrated in Fig. 1.

*E-mail: vladimir.shevchenko@ukaea.org.uk

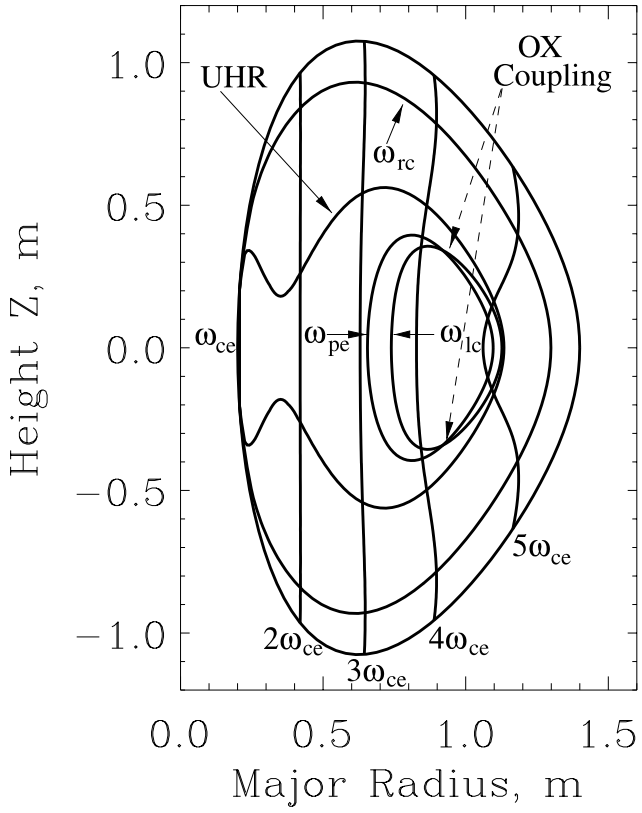

Fig. 1. Poloidal cross section showing cutoffs and resonances for 60-GHz electromagnetic wave with $N_{\parallel} = 0.42$. MAST plasma: $I_p = 0.6$ MA, $I_{rod} = 2.2$ MA, $n_{e0} = 4.8 \times 10^{19}$ m^{-3}, parabolic plasma and current density profiles. Note the poloidal field (B_{PF}) effect on the EC harmonic shape. This is due to the strong TF (B_{TF}) dependence on the major radius (R), typical for STs, $B_{TF} \sim R^{-1}$. As a result, $B_{PF} \ll B_{TF}$ on the HFS and $B_{PF} \sim B_{TF}$ on the LFS.

EBWs are considered to be a promising means of plasma heating and CD in STs. EBWs are predominantly electrostatic waves, and they cannot propagate in vacuum. However, EBWs can be coupled to the vacuum electromagnetic waves via MC mechanisms. These mechanisms allow the thermal EBW emission (EBE) to escape the plasma, and conversely, EBWs can be excited within the plasma with the externally launched X-modes or O-modes from the low field side (LFS) of the machine. By the reciprocity theorem[6] and MC symmetry principles,[7] both processes are completely symmetrical until nonlinear effects of the plasma-wave interaction become significant. Extensive ray-tracing modeling and thermal EBE (16 to 67 GHz) measurements suggest the preferable operating frequency for efficient EBW heating and CD must be in the range of the fundamental EC resonance or its lower harmonics.[8,9] This requires a high-power RF source in the range of 16 to 28 GHz. A lower-frequency EBW CD system is presently under consideration for future implementation in MAST. In contrast to neutral beam CD, the EBW absorption and CD efficiency remain high even far off the magnetic axis. This makes a combined (neutral beam and EBW) CD system an attractive scheme to generate and sustain plasma noninductively in STs. A 60-GHz (~1-MW) gyrotron complex is available in MAST. It is equipped with a steerable 7-beam launching system. Despite the fact that the operating frequency is far from optimum, a number of physical processes can be studied with the existing experimental setup.

EBW may also be used in the plasma start-up phase because EBW absorption and CD efficiency remain high even in relatively cold plasmas.[1] A 28-GHz EBW start-up system has been designed and is now being commissioned in MAST (Ref. 10). According to our modeling, EBW can generate plasma current up to 100 kA during the plasma start-up phase, giving the prospect of a fully noninductive plasma start-up scenario.

II. EBW-MODE EXCITATION IN TOKAMAK PLASMA

The EBW-mode can be excited in the plasma by externally launched electromagnetic waves using different MC mechanisms. For instance, the slow X-mode launched from the HFS of the tokamak converts totally into the EBW-mode at the upper hybrid resonance (UHR). This type of MC is the most effective mechanism of EBW excitation,[11,12] and it has been used in our experiments on COMPASS-D (Ref. 2) and in some other machines.[13,14] Despite an almost complete X-B MC at UHR, this method has a limited application in tokamaks because of plasma density restrictions. The density limit arises from the UHR accessibility requirements at the plasma boundaries:

$$\omega_{ce}^{HFS} > \omega_{RF} > \omega_{ce}^{LFS} \tag{1}$$

and

$$\omega_{RF} > (\omega_{pe}^2 + \omega_{ce}^2/4)^{1/2} - \omega_{ce}/2 \ , \tag{2}$$

everywhere along the X-mode beam path. A noninductive plasma start-up scenario based on this method will be discussed in Sec. VII.

In contrast, the EBW excitation based on the O-X-B MC from the LFS has a low density limit, which arises from the mode-coupling requirements:

$$\omega_{ce}^{LFS} < \omega_{RF} < \omega_{pe} \ , \tag{3}$$

i.e., for the EBW-mode to exist the RF frequency must be higher than the EC frequency at the O-mode entrance into the plasma and the O-mode cutoff must be present in the plasma. A detailed analysis of the O-X-B MC problem can be found in Refs. 15 and 16. Here we restrict ourselves to a discussion of practical implications of the O-X-B coupling theory in STs. According to this theory

the O-mode first converts into the slow X-mode near the O-mode cutoff, and then the slow X-mode is totally converted into the EBW-mode at the UHR. The O-X stage is the most demanding part of this process because it requires the O-mode cutoff and the slow X-mode cutoff to be coincident on the RF beam path. In a cold plasma approximation, the spatial location of the O-mode cutoff $\omega_{RF} = \omega_{pe}$ depends only on the local plasma density for any particular frequency ω_{RF} of wave injected into the plasma. The slow X-mode cutoff ω_{lc} depends also on the local plasma density, magnetic field, and the parallel component $N_{\parallel}$ of the refractive index:

$$\omega_{lc} = [\omega_{pe}^2/(1 - N_{\parallel}^2) + \omega_{ce}^2/4]^{1/2} - \omega_{ce}/2 \ . \qquad (4)$$

The dependence on $N_{\parallel}$ allows us to manipulate the spatial location of the O-X MC zone by varying the poloidal launcher position and RF launch angles. Figure 1 illustrates a poloidal cross section of the MAST plasma with the cutoff and resonance layers calculated for the 60-GHz wave with $N_{\parallel} = 0.42$. There are two crossing points, symmetrical against the midplane, between O-mode and X-mode cutoff lines where the O-X coupling is total. Away from these points the coupling efficiency decays exponentially. Obviously, an identical picture can be obtained for $N_{\parallel} = -0.42$, so there are four possible RF launch configurations for this set of parameters. In order to obtain the external RF launch angles for these points, one can use a plane-stratified plasma approximation[15,16] for a rough estimate. By Snell's law, $N_{\parallel}$ is conserved in that case and $N_{\parallel opt}^2 = \omega_{ce}/(\omega_{ce} + \omega)$, where ω_{ce} is evaluated at the O-X conversion point.

In order to obtain accurate values for the optimal launch angles and the wave polarization in toroidal geometry, the O-mode must be traced back from the conversion point to the plasma boundary. In practice it is easier to solve the direct problem of wave propagation from the existing antenna to the O-mode cutoff in the range of launch angles around the analytical solution. A typical map of the O-X-B mode-coupling efficiency is shown in Fig. 2. Here the one-dimensional (1-D) full-wave numerical treatment of the O-X mode-coupling problem[17] has been used near the MC layer. There are always two MC windows corresponding to $\pm N_{\parallel opt}$ for every chosen poloidal location of the launcher (only $+N_{\parallel opt}$ windows are plotted on Fig. 2). For fixed RF frequency and given EC harmonic, the angular width of the O-X window depends only on the density gradient at the conversion layer. The optimal polarization is close to circular for both windows but with opposite direction of rotation. The electric field vector rotates clockwise for the $+N_{\parallel opt}$ launch and counterclockwise for the $-N_{\parallel opt}$ launch. Thus the RF launching antenna must be steerable both poloidally and toroidally, and it must allow polarization control.

A 1-D consideration of the mode-coupling problem suggests that the coupling process is completely identical above and below the midplane of the torus. However, further studies of the O-X MC have shown the importance of 2-D effects in toroidal plasmas.[18,19] It appears that local O-X and X-O MC processes are not entirely symmetrical. In toroidal plasmas the X-O (emission from the plasma) coupling efficiency is always higher than O-X (RF injection into the plasma) if the mode transformation is happening above the midplane; and vice versa, the O-X process is predominant (up to 15% in MAST) over X-O below the midplane. Moreover, the O-X MC efficiency above/below the midplane is exactly equal to the X-O MC efficiency below/above the midplane for the plasma layers at the same distance from the midplane and for the same $N_{\parallel}$. Because of such global symmetry the reciprocity theorem[6] is not violated.[18] In the vicinity of the midplane, the 2-D effects are vanishing and the

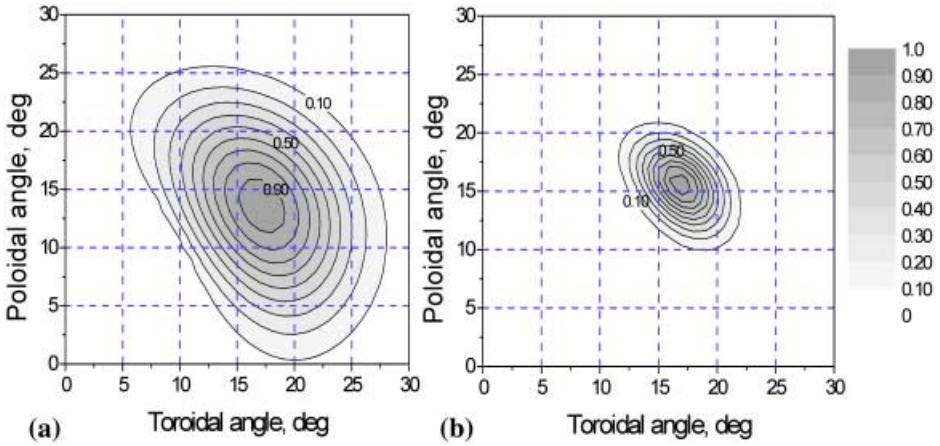

Fig. 2. The O-X-B MC window (positive $N_{\parallel}$) calculated for the 60-GHz launcher located 22.5 cm below the midplane in MAST: (a) high-density ELM-free H-mode, and (b) high-density L-mode plasma. Contours indicate 10% steps in conversion efficiency, i.e., 0.5 means 50% conversion efficiency, etc.

1-D treatment of the MC problem can be applied with good accuracy. These 2-D effects have not been verified experimentally yet, but they are certainly important for the design of EBW heating and CD systems with off-midplane RF launch.

EBWs may also be excited with the X-mode launched from the LFS. In this case the fast X-mode tunnels through the evanescent layer between the right-hand cutoff and the UHR and then couples to the slow X-mode, which is mode-converted into EBW-mode at the UHR. A theoretical analysis of the X-B tunneling problem based on the full-wave treatment has been summarized in Refs. 20 and 21. This scheme has been proposed for EBW excitation in STs (Ref. 22). Further theoretical and experimental studies of X-B tunneling can be found in Refs. 23, 24, and 25. In this paper, we concentrate on the O-X-B MC process successfully demonstrated in plasma heating experiments on W7-AS (Ref. 26). This mechanism was proposed for plasma heating in MAST (Ref. 27) and the inverse process has also been proposed as a diagnostic.[28] We use a full-wave 1-D mode-coupling approach, which associates the MC process with the singularity of the cold plasma wave equation in the UHR, with no references to the Wentzel-Kramers-Brillouin theory. It was shown[17] that this approach, originally formulated for the case of strongly inhomogeneous plasmas,[29] can be used in magnetized plasmas regardless of the inhomogeneity scale length. In fact, depending on the inhomogeneity scale length, the full-wave solution describes the X-B tunneling, O-X-B coupling, and various combinations of both processes.[30–35] Some of the aspects of this approach in our modeling are discussed in Sec. V.

III. 60-GHz RF HEATING SYSTEM IN MAST

The RF heating system in MAST consists of seven 60-GHz gyrotrons, 200 kW each, with a pulse length up to 5 s. The gyrotrons operate in TE_{02} mode. They are connected to the main TE_{01} transmission lines via mode correctors and TE_{02}-TE_{01} converters. The transmission lines are made up from 3-m-long sections of circular smooth waveguide 30 mm in diameter. Typical lines have four bends and are from 30 to 40 m in length. At the entrance to the machine the TE_{01} mode is converted into the HE_{11} mode in two steps with TE_{01}-TE_{11} and TE_{11}-HE_{11} mode converters. Orientation of the output linear polarization can be controlled by the orientation of the TE_{01}-TE_{11} ("snake") mode converter. The HE_{11} part of the transmission line is made up from circular corrugated waveguide 30 mm in diameter. The fused silica vacuum window is incorporated into the waveguide. The transmission line ends up with a mouthpiece antenna inside the vacuum vessel. The measured loss in a complete line is ~20%.

A quasi-optical launcher assembly is located inside the vessel (see Fig. 3). It provides the desired polarization and beam-steering capabilities for all beams. There are three quasi-optical components in every beam line. The first is a grooved mirror-polarizer with a sinusoidal-shaped front face that modifies the incident linear polarization into the desired elliptical polarization depending on the orientation of the TE_{01}-TE_{11} mode converter. If the incident polarization of the beam is parallel or perpendicular (±45 deg from vertical) to the grooves of the polarizer, the output polarization is linear. If the polarization is vertical or horizontal, the output polarization is right-hand or left-hand circular. In all intermediate cases the output polarization is elliptical. The second component is a paraboloidal mirror that forms a Gaussian beam with a beam waist radius of 25 mm. This mirror also provides beam steering in the poloidal direction by revolution about the optical axis of the incident beam. The third mirror is flat and provides beam steering in the toroidal direction. Beam lines are grouped as 2-3-2 according to their position with respect to the midplane. Each group has a common remote control for poloidal and toroidal steering. That is because the optimal launch angles are dependent on the vertical position of the launcher and independent of the toroidal position. The poloidal steering range is about ±13 deg for every group of beams, and the toroidal steering range is ±24 deg with a beam divergence of ~3.5 deg. After the installation of the launcher, the relative orientation of the mirrors has been calibrated with the use of photogrammetry technology and low-power RF cross-channel tests at several aiming angles. These allowed us to obtain the relative orientation of the RF beams to an accuracy of ±2 deg.

IV. EBW DIAGNOSTICS

By the reciprocity theorem,[6] thermal EBE escaping from the plasma can provide useful input, over a wide range of frequencies, for the study of optimum conditions for mode coupling and absorption. Extensive EBE studies in the frequency range 16 to 67 GHz, covering the first six EC harmonics, were conducted in MAST (Refs. 8, 36, and 37). In our studies we employed two radiometers. One of them was originally developed for the COMPASS-D tokamak.[38] It is a 12-channel heterodyne radiometer covering the frequency range from 54 to 66 GHz with 1 GHz spectral and 10 μs temporal resolution. Because the radiometer frequency range is close to 60 GHz, the heating antennas and transmission lines can be used for EBE studies. In order to keep the mode purity, the radiometer is connected to the one of the heating TE_{01} transmission lines via a chain TE_{01}-TE_{11}-HE_{11}-TE_{01}^{rect} of mode converters. Such an arrangement provides exactly the same polarization and beam pattern for the emission measurements as in heating experiments.

The second radiometer is a frequency-scanning radiometer,[39] which covers the frequency range 16 to

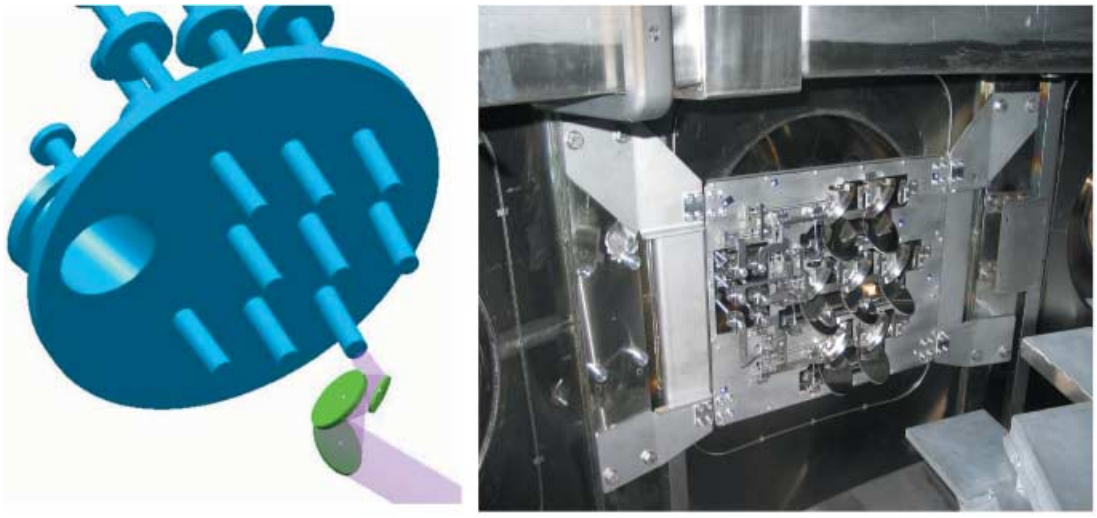

Fig. 3. Seven-beam steerable RF launcher in MAST: (a) single beam path diagram and (b) photograph of the launcher installed in the MAST vessel.

60 GHz. It consists of three frequency-sweepable heterodyne receivers operating in the bands: 16 to 26 GHz, 26 to 40 GHz, and 40 to 60 GHz. Each receiver has an independent voltage-controlled oscillator and a harmonic mixer. The receivers are attached to a single receiving antenna via frequency-selective power splitters. The receiving antenna is equipped with a periscopic mirror system allowing manual control of the antenna viewing angles. The steering range of the antenna is about ± 30 deg in the toroidal direction and ± 20 deg in the poloidal direction. The radiometer receives only linear polarization. The orientation of the received polarization is chosen by a polarization rotator behind the antenna. The frequency scan is arranged over 32 sequential frequency steps. The duration of each step is 20 μs, so the whole spectrum is measured over 96 frequency channels every 0.64 ms. A typical spectrogram of EBE from high-density plasma in MAST is presented in Fig. 4. In STs the thermally emitted EBW spectrum usually contains a series of well-separated maxima corresponding to overdense EC harmonics.[28,40] The minima in the EBW spectrum occur at coincidences of the UHR and EC harmonic (see Fig. 7), and are thus determined by the magnetic field and electron density. Two minima (stars in Fig. 4), estimated from the measured plasma density[41] and reconstructed magnetic field profiles, show good agreement with EBE measurements. The emission from ω_{ce} and $2\omega_{ce}$ harmonics can be clearly seen during the shot. In this shot, the UHR, where the B-X MC occurs, is gradually shifted toward higher toroidal field (TF) because of plasma compression in the direction of the major radius. As a result the ω_{ce} and $2\omega_{ce}$ emission is monotonically drifting to higher frequencies. Harmonic

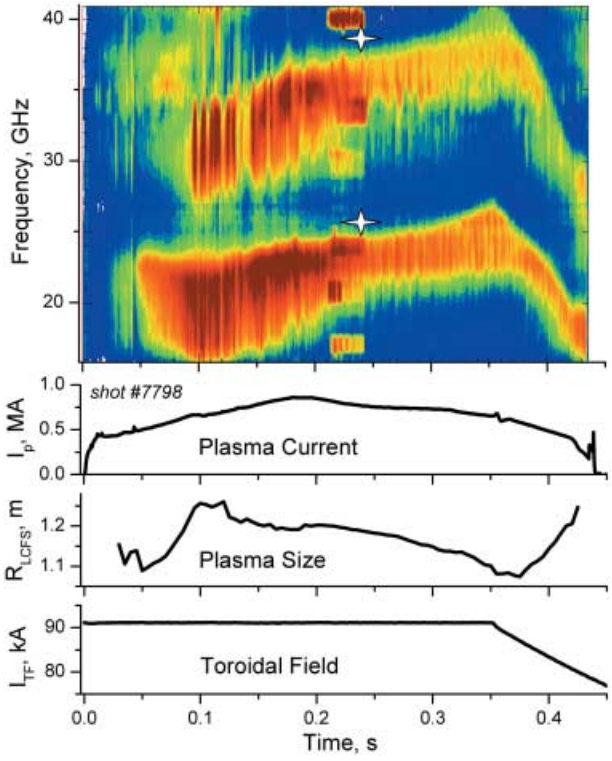

Fig. 4. Thermal EBE spectrogram measured via B-X-O MC during high-density plasma shot #7798 in MAST. Antenna viewing angles are +14 deg in the poloidal direction and +15 deg in the toroidal direction. Red areas correspond to higher EBE intensity. Stars indicate positions of minima of EBE estimated from experimental data. RF power was injected between 0.21 and 0.24 s. B_{TF} (T) = 4.8 I_{TF}/R (MA/m).

frequencies quickly drop down after 0.35 s because of the TF decrease. In general, the observed spectra are consistent with the theory of mode coupling and EBW propagation in ST plasmas. However, some features of the EBW spectrum, especially during H-mode,[8,36] still require further studies.

A special probe, along with a spectrum analyzer, has been developed to study parametric decay effects associated with EBW heating in MAST. The probe consists of two antennas incorporated into a standard reciprocating probe head (see Fig. 5). It can be moved into the vessel to a specified distance from the plasma boundary in the midplane. The probe also allows axial rotation in the range of ±45 deg. This is important for the loop antenna that can be aligned perpendicular or parallel to the local magnetic field. The loop antenna is predominantly sensitive to the magnetic component of the lower-hybrid (LH) wave slowed down in the peripheral plasma. The second antenna is of an electrostatic type and it detects the electric component of the incident LH wave. Both antennas are connected to a frequency-scanning spectrum analyzer via impedance-matching isolating transformers. The spectrum analyzer provides full spectrum measurements from 76 to 545 MHz with ~10-MHz resolution every 1.2 ms. The use of these specifically developed diagnostic tools in EBW heating experiments in MAST is discussed in Sec. VI.

V. EBW MODELING

The optimum choice of frequency and launch configuration for EBW heating and CD is a key issue for future applications in MAST. The propagation and dispersion of EBWs is a complicated function of electron temperature and magnetic field in the plasma. Magnetic field topology in STs is characterized by relatively rapid variations of poloidal and toroidal components over the major radius. This fact makes the task of EBW heating and CD optimization multiparametric. Modeling was conducted in a parametric space including variations of heating frequency over the fundamental and higher harmonics, different launch polarization, and vertical position Z of the launcher. The goal was to find the optimal parameters for off-axis CD and for central heating and CD. A major advance in the integrated modeling of EBW, involving a suite of codes, has been achieved.

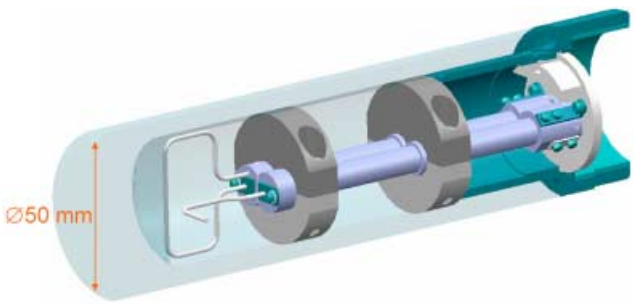

Fig. 5. Cross section of the LH probe used for the study of parametric decay.

A Gaussian beam incident upon the plasma is first Fourier decomposed, and propagation of each Fourier component in vacuum and plasma is then considered separately. The EBW excitation in the plasma is then treated as a full-wave 1-D mode-coupling problem in slab geometry as described in Ref. 17. Calculations are performed in Cartesian coordinates with the x-axis perpendicular to the plasma boundary and with the origin located at the point where the beam center crosses the plasma surface. According to this approach the EBW is excited in the vicinity of the UHR where the cold plasma approximation for the electromagnetic mode is violated. To describe the MC it is sufficient to find a solution of the cold plasma wave equation vanishing in the high-density evanescent region and matching to the incident and reflected waves at the plasma edge. The UHR is a singular point of the wave equation. In the immediate vicinity of this point, the solution can be presented analytically, and the theory gives a rule for choosing its proper branch. The singularity of the x-component of the electric field is a pole and its residue determines the complex Wentzel-Kramers-Brillouin amplitude of the outgoing EBW. This approach does not require applicability of the Wentzel-Kramers-Brillioun approximation for the electromagnetic mode and includes both the O-X-B MC and the direct X-B tunneling. The coupling code solves the cold plasma wave equation for each Fourier component of the antenna beam using a Runge-Kutta method and finds the required residue. The EBW electric field distribution for the whole beam is then computed at the flux surface close to the UHR with the use of the inverse Fourier transformation. The electric field distribution serves as the starting condition for the EBW beam in a ray-tracing code. Thus, the initial conditions for EBW rays are prescribed unambiguously for the specified launch parameters, including the beam width, divergence, polarization, and antenna position.

Then propagation of the EBW is computed using the EBW ray-tracing code, which implements a fully electromagnetic hot plasma dispersion function during the preliminary stage of the RF launch optimization. EBW absorption along the rays is calculated using a relativistic electrostatic approximation.[42] The ray-tracing data (wave vector and polarization at every point in each ray) are then used in the BANDIT code[43] in a self-consistent, relativistic three-dimensional Fokker-Planck treatment to calculate the heating and driven current profiles. BANDIT reproduces the ray-tracing code's absorption profiles and then calculates disturbances to the distribution function on each flux surface to give a driven current profile, which in general is very localized. Such an

optimization incorporating relativistic absorption along nonrelativistic EBW rays takes only a few minutes on a moderate workstation with a single processor. The fully relativistic electrostatic dispersion relation is used in the EBW ray tracing only at the final stage of heating and CD simulations because it typically requires 20 times longer run time in comparison with nonrelativistic ray tracing. The use of the EBW modeling tools in experiments in MAST is discussed in the next sections. Here we summarize the potential of EBW CD in MAST based on our modeling results.

The main objective for the EBW CD system is to provide efficient off-axis CD radially localized at $r/a \sim 0.7$. The central current is supposed to be sustained by neutral beam injection. Figure 6 illustrates EBW CD capabilities over the minor radius. The target plasma used in our modeling has a flat density profile with $n_{e0} = 4.5 \times 10^{19}$ m^{-3} and a parabolic electron temperature profile with $T_{e0} = 4$ keV. It was assumed for optimization purposes that the vertical position Z of the launcher can be chosen and the RF frequency can be varied within the range of the fundamental resonance. As seen in Fig. 6 the CD efficiency remains almost constant at ~0.15 A/W over the radii r/a from 0 to ~0.7. Then it crosses 0 at $r/a \approx 0.75$ and becomes negative in the peripheral region, where Ohkawa current dominates over Fisch-Boozer current. Thus, for the neutral beam injection CD assist the optimal frequency is ~18.5 GHz with the launcher positioned at about $Z = 75$ cm above/below the midplane for co-/counter-CD. However, if the broader applications are considered for EBW CD in MAST (such as a fully noninductive plasma formation, localized current density control over the radius, etc.), a few switchable launchers must be employed allowing central and midradius CD. The modeling suggests the preferable operating frequency for efficient EBW heating and CD must be in the range of the fundamental EC resonance or its lower harmonics.[8] This requires a high-power RF source in the range of 16 to 30 GHz. A lower-frequency EBW CD system is presently under consideration for future implementation in MAST.

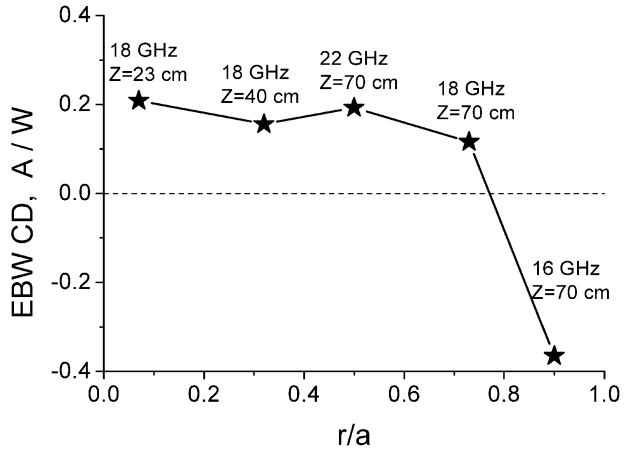

Fig. 6. Predicted EBW CD efficiency over minor radius in MAST with 1-MW injected power. Relativistic effects included. Frequency and vertical position Z of the launcher are indicated.

VI. PROOF-OF-PRINCIPLE EBW HEATING EXPERIMENTS

The experiments were conducted at 60 GHz with injected RF power up to 0.8 MW. The first stage of the O-X-B MC process occurs in the $\omega_{RF} = \omega_{pe}$ layer, and the conversion efficiency depends mainly on the local density gradient scale length. Thus, high-density plasma with a steep density gradient near the plasma cutoff, where $n_e \sim n_c = 4.5 \times 10^{19}$ m^{-3}, is required for the 60-GHz experiments. This constraint pushes plasma to the limit of MAST operational space. Therefore, three different plasma scenarios have been developed especially for these experiments.[44] Figure 7 represents the midplane topologies of cutoffs and resonances plotted for these scenarios. A magnetic field reconstruction and electron density profiles, measured with a high resolution Thomson scattering diagnostic,[41] have been used in the calculations of these topologies. Measured density profiles were not smoothed or filtered; therefore, nonmonotonic features can be seen on cutoffs and resonances.

The first scenario (Fig. 7a) is based on the high-density edge-localized mode (ELM)-free H-mode. It offers a relatively broad (±5 deg) O-X-B MC window because of a high-density gradient in the conversion zone, but EBW absorption, as predicted by modeling, is expected to be very peripheral ($r/a \sim 0.9$). As the O-X-B MC occurs in relatively cold plasma layers close to the separatrix, nonlinear phenomena were anticipated in this scenario.[14,26] The electric field of the wave approaching the UHR increases dramatically and at some level can cause nonlinear effects, in particular, parametric decay instability. Parametric decay can lead to redistribution of the incident power between plasma species and cause anomalous reflection, especially when excited at the plasma edge.

Radio-frequency power is expected to be deposited at high EC harmonics (between $5\omega_{ce}$ and $6\omega_{ce}$), leading to peripheral absorption and ineffective heating in this scenario. Nevertheless, clear evidence of the MC process was obtained by nature of the fact that parametric decay waves originating from the UHR were observed using the LH probe (see Sec. IV). Figure 8a illustrates a strong plasma emission enhancement of ~134 MHz during the RF pulse when plasma reached the overdense state. The enhanced emission is very localized in frequency (Fig. 8b). The half-width of the spectral peak is ~10 MHz. Because the spectral maximum is close to the LH resonance frequency in the UHR region for 60 GHz, we identify this

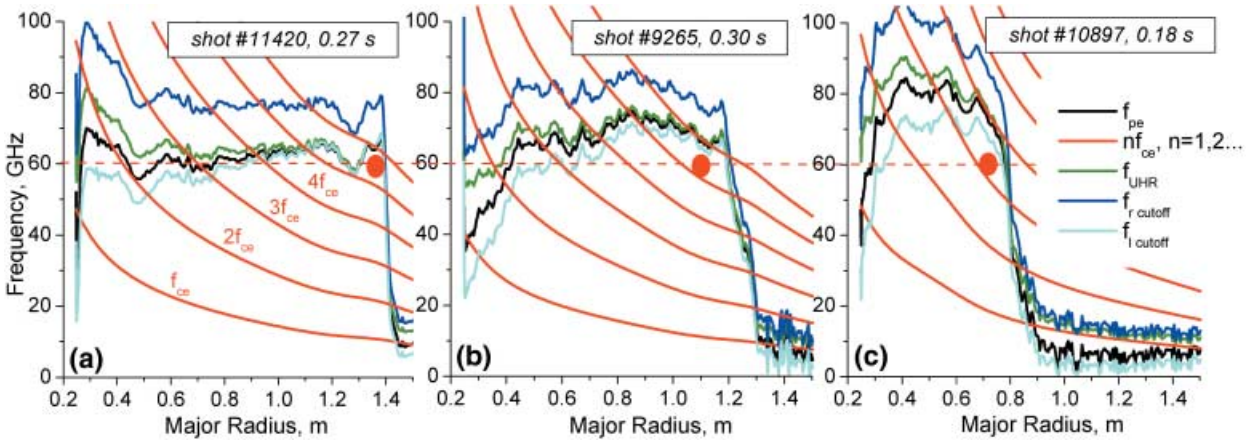

Fig. 7. Plasma scenarios developed for EBWH experiments. Midplane resonances and cutoffs illustrate RF accessibility to the core plasma. Power deposition is indicated by red spots: (a) ELM-free H-mode, (b) sawtoothing H-mode, and (c) ohmic H-mode.

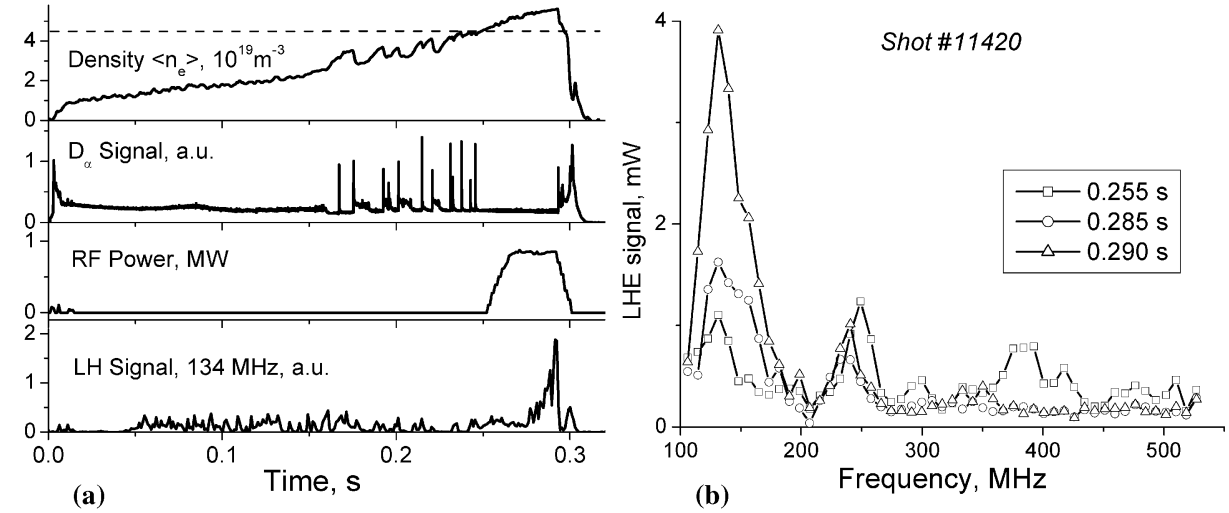

Fig. 8. (a) Line-averaged plasma density, D_α signal, and RF power in 60-GHz EBW heating experiment with ELM-free H-mode. The plasma becomes overdense, i.e., MC becomes possible, when plasma density is above the dashed line. Note the strongly increased LH signal peaked at 134 MHz during the RF pulse when plasma reached the overdense state. The probe position is ~5 cm outside the last closed flux surface. (b) LH emission spectra during the RF pulse.

radiation as generated by the parametric decay instability occurring in the UHR.

A theoretical study of parametric decay of the incident upper-hybrid wave into another upper-hybrid wave plus LH wave has been conducted in collaboration with the Ioffe Institute. The power threshold and growth rates of the absolute decay instability were evaluated for the specific conditions of low magnetic field typical for the ST. According to Ref. 45, the threshold for the fundamental mode of the parametric decay can be estimated from the following expression:

$$\frac{P^*_{\mathrm{UHR}}}{\pi\rho^2}\left(\frac{\mathrm{W}}{\mathrm{cm}^2}\right) = 2\times 10^{-3}\left(\frac{\mathrm{W}}{\mathrm{cm}^{2/3}\,\mathrm{T}^{1/3}\,\mathrm{GHz}^{1/3}\,\mathrm{eV}^{13/6}}\right) \times \frac{f^{1/3}T_{eff}^{11/12}T_e^{5/4}B^{1/3}}{L^{4/3}}\ , \qquad (5)$$

where $T_{eff} = T_e + 4T_i$, ρ is the e^{-1} (electric field) radius of the heating beam spot, and L is the inhomogeneity scale: $L^{-1} = \mathrm{grad}(n_e)/n_e + 2\omega_{ce}^2/\omega_{pe}^2\,\mathrm{grad}(B)/B$. All plasma parameters are taken at the UHR. For typical

MAST parameters at $f = 60$ GHz, $T_i \approx T_e = 140$ eV, $B = 0.38$ T, and $L = 3$ cm, the parametric decay (1) can arise at $P^*_{\mathrm{UHR}}/(\pi\rho^2) \approx 260$ W/cm^2, i.e., if the pump power exceeds $P^*_{\mathrm{UHR}} \approx 80$ kW in any beam spot of $\rho \approx$ 10-cm radius. The obtained value allows us to estimate the coupling to EBW to be no less than 50% in at least one of the beams, because beam overlapping is negligible.

The second scenario (Fig. 7b) is based on a sawtoothing H-mode plasma, in which a high-density gradient zone allowing the O-X-B conversion appears deeper into the plasma. In this scenario the density gradient is very steep in the range up to 2×10^{19} m^{-3} and has a relatively moderate value at higher densities. This allows us to shift the plasma cutoff (O-X conversion layer) by 10 to 15 cm deeper into the plasma, avoiding interception by the upper EC harmonic. As a result the MC window is narrower (±3 deg) in this case, but the EBW power deposition can reach $r/a \sim 0.6$ (see Fig. 9).

A TF scan has been conducted on a shot-by-shot basis to optimize heating in this scenario. The aim was to obtain EBW penetration between the $5\omega_{ce}$ and $6\omega_{ce}$ harmonics (see Fig. 7b) as deep as possible. Unlike the first scenario (Fig. 7a), in this case, the cutoffs and resonances were not "frozen" during RF injection, because of MHD activities. Hence, the MC layer location was not known accurately enough. The EBE enhancement from the lower EC harmonics during RF injection has been used as a diagnostic of the EBW-plasma interaction. The shape of the spectrum and the relative signal increase provide information on the MC efficiency and the RF penetration depth. For example, the spectrogram in Fig. 4 illustrates the case where no noticeable EBE enhancement has been observed. The TF scan has shown that the EBE enhancement (see Fig. 10) during RF injection has a well-pronounced maximum when the O-mode cutoff is located at about two-thirds of the distance between the $5\omega_{ce}$ and $6\omega_{ce}$ harmonics. This scenario with optimized TF has provided some evidence of plasma heating during RF power injection. The O-X-B MC (and, consequently, heating) is strongly modulated by sawteeth and ELMs; hence, the effect is better seen after averaging over three shots. Figure 11 indicates an increase of ~10% of the total plasma energy (EFIT code) during the RF pulse with an average injected RF power of ~0.25 MW. The total heating power (neutral beam injection + ohmic) in these shots was ~3 MW. It should be noted that no parametric decay has been observed in sawtoothing H-mode. This can be explained by the fact that the MC occurs in the deeper plasma layers where the temperature is higher than in ELM-free H-mode. Equation (5) gives an approximately quadratic dependence on electron temperature, so the power threshold was not exceeded in this scenario.

In the third scenario, high-density ohmic H-mode (Fig. 7c) is achieved by plasma compression in major radius. Because plasma is compressed into a higher magnetic field, $r/a \sim 0.4$ becomes accessible transiently at $3\omega_{ce}$ and then at $2\omega_{ce}$ during the compression process. The MC window (±1.5 deg) is very restrictive in this case, hence the thermal EBE from $3\omega_{ce}$ was used for the launch optimization (Fig. 12). EBE measurements at 60.5 GHz show two distinctive maxima in time intervals 0.17 to 0.2 s and 0.22 to 0.25 s, corresponding to accessibility windows for $3\omega_{ce}$ and then $2\omega_{ce}$ (Fig. 13). Thus the RF pulse timing was chosen to cover both time intervals. The soft X-ray (SXR) signal was practically doubled during the RF pulse in comparison with the ohmic plasma, as illustrated in Fig. 14. During the intervals when $3\omega_{ce}$ and $2\omega_{ce}$ become accessible, the SXR signal shows a higher rate of increase. Thomson-scattering measurements[41] at 0.18 and 0.2 s show an increase of ~10% in electron temperature in the RF-heated shots in comparison to the ohmic shots (Fig. 15). EBW heating effects can also be seen from the total plasma energy behavior during RF injection, as illustrated in Fig. 16. Here three plasma shots with similar parameters are compared: one without RF injection and the other two with RF injection of different power and RF-pulse duration. One can see a well-pronounced (up to 30%) increase of the total plasma

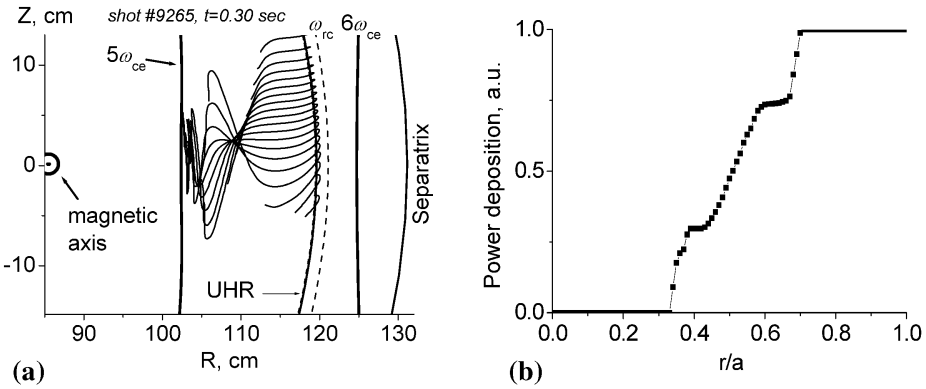

Fig. 9. Ray-tracing modeling results for sawtoothing H-mode plasma, upper launcher: (a) poloidal projection of EBW rays and (b) power in the beam normalized to the incident power as a function of radius.

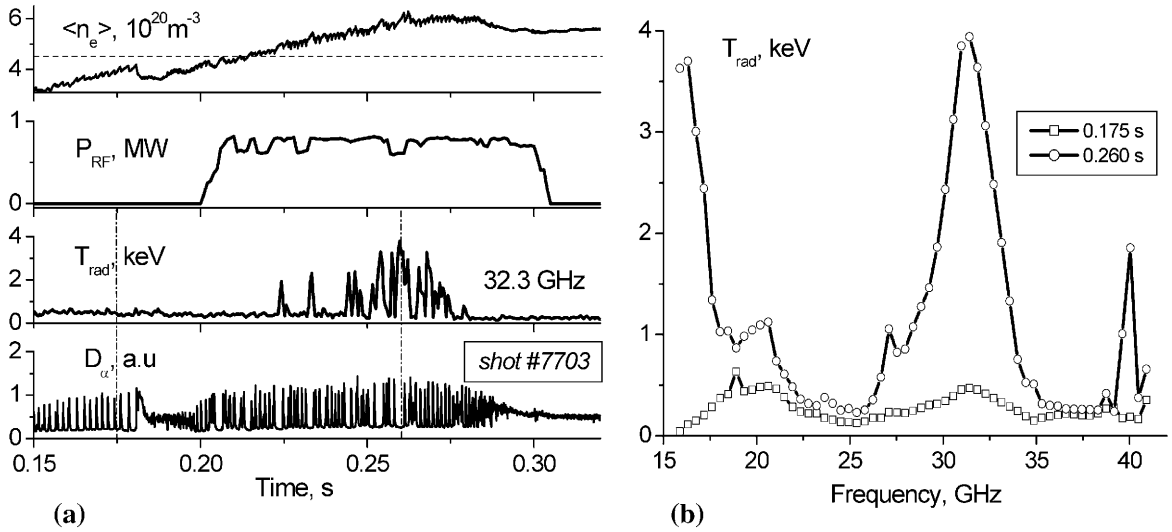

Fig. 10. (a) Plasma density, RF power, radiative temperature, and D_α signal in sawtoothing H-mode at optimized TF. Note the radiative temperature enhancement between ELMs during RF injection. (b) EBW radiative temperature profiles measured between ELMs: 0.175 s = squares, 0.26 s = circles. The narrow peak at 40 GHz is due to 60-GHz stray radiation mixing at the third harmonic of the local oscillator.

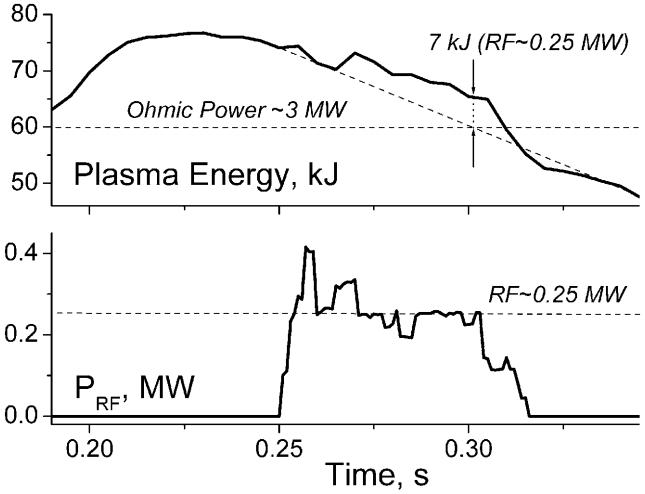

Fig. 11. EBW heating results in sawtoothing H-mode averaged over three plasma shots: #9262, #9264, and #9267.

energy in the case of ~600-kW RF injection. The mode-coupling efficiency for this scenario can be estimated from EC emission measurements at the same viewing angle as for RF launching; see shot #10639 in Fig. 13. During the initial phase (0.03 to 0.04 s), the plasma has flat density ($n_e \approx 1.6 \times 10^{19}$ m^{-3}) and temperature ($T_e \approx$ 400 eV) profiles as measured with Thomson scattering. The second EC harmonic is not obscured by the cutoff, and it is optically "black" for the X-mode during this time interval. The antenna receives right-handed circularly polarized waves as it is optimized for the oblique O-mode launch. Hence, only half the power of the linearly polarized X-mode emission is detected. By contrast, the O-mode emission, escaping via the B-X-O MC, during the overdense phase (0.1 to 0.3 s) is detected in full. The temperature of the plasma layer responsible for the emission at 0.18 s can be estimated from Figs. 7c and 15. One can see that EBE originates at $R \approx 0.7$ m, which gives $T_e \approx 500$ eV. Comparing amplitudes of the EC signal at 0.035 s and at 0.18 s (shot #10639 in Fig. 13), we conclude that the mode-coupling efficiency is ~90% during H-mode periods (maxima of the EBE signal) and ~25% during L-mode periods (minima of the EBE signal). Averaged mode-coupling efficiency for the $3\omega_{ce}$ resonance is close to 50% with ~10% error bar. Unfortunately, it was not possible to use the LH probe in this scenario because the plasma boundary was moving during the shot.

VII. 28-GHz START-UP SYSTEM

It has been shown experimentally that EBW CD excited with the X-mode launched from the HFS is capable of producing a substantial amount of current,[2] which could possibly sustain plasma stability during plasma current flat top. Obviously, the above scheme has a very limited application in STs because plasmas are typically well overdense ($\omega_{pe} \gg \omega_{ce}$) in the core because of relatively low TFs used in STs. However, such a scheme can be employed during the plasma start-up phase. A noninductive plasma current start-up

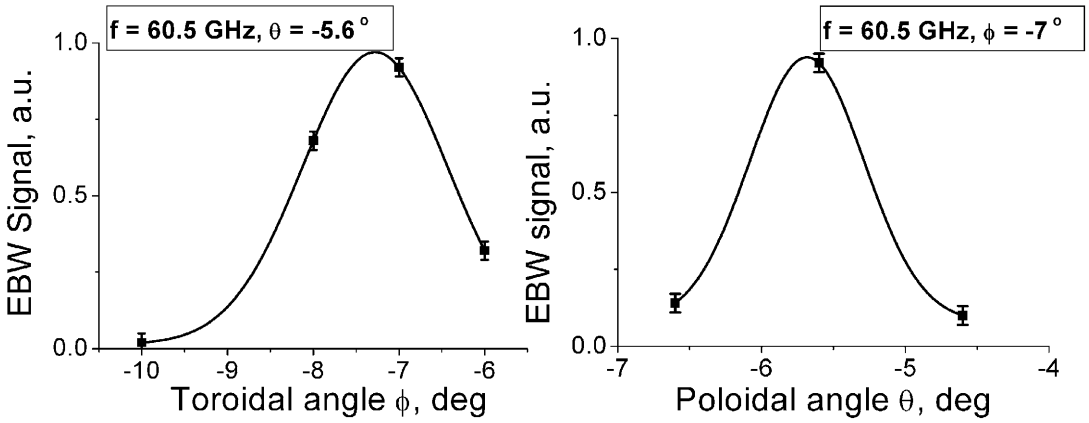

Fig. 12. Launch angle optimization for injection into ohmic H-mode plasma using $3\omega_{ce}$ EBE measurements at 60.5 GHz through the upper ($Z = 7.5$ cm) launcher (see Fig. 3).

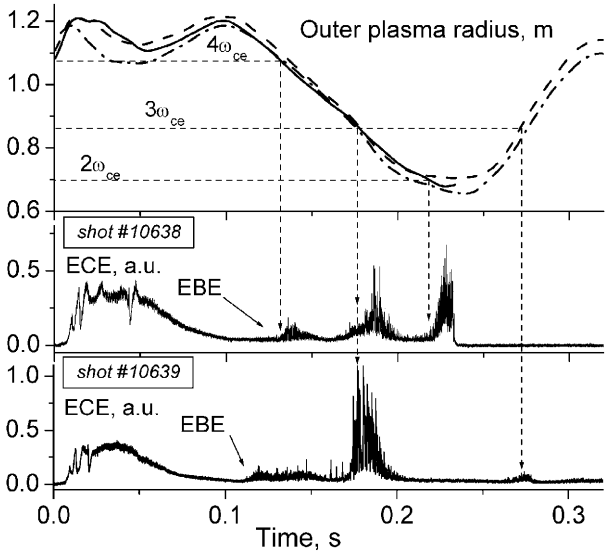

Fig. 13. Plasma boundary dynamics in high-density ohmic H-mode during plasma compression: shot #10638 = solid line, shot #10639 = dashed line, and RF-heated shot #10874 = dash-dot line. As the plasma boundary moves into the higher magnetic field during compression, EBE (60.5 GHz) comes first from $4\omega_{ce}$, then from $3\omega_{ce}$, and finally from $2\omega_{ce}$. The $2\omega_{ce}$ emission is seen when the outer radius is smaller than 0.7 m. Plasma is usually disrupted when compressed down to 0.7 m without RF injection (shot #10638). No disruption was observed with RF injection (shot #10874).

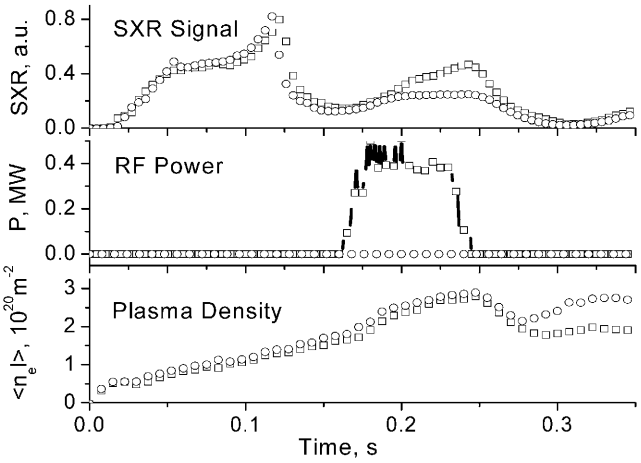

Fig. 14. SXR signal, RF power, and line-integrated plasma density in RF-heated shot (squares) and ohmic shot (circles). Note a strong increase of SXR signal during RF injection.

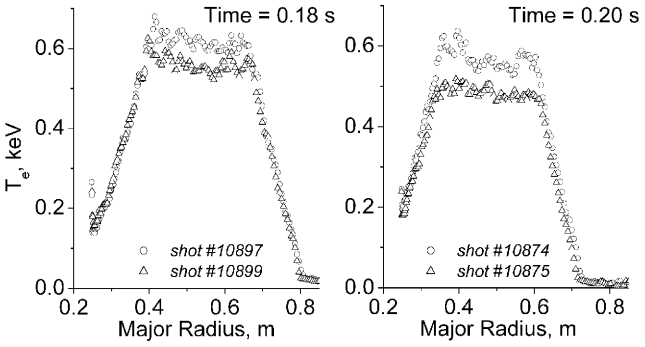

Fig. 15. Electron temperature profiles measured by Thomson scattering in RF-heated (shots #10897 and #10874) and ohmic (shots #10899 and #10875) plasmas at 0.18 s and at 0.2 s, respectively.

scenario based on EBW CD at 28 GHz has been proposed for MAST (Ref. 10). The scheme consists of three sequential stages (see Fig. 17):

1. First, the ordinary polarized RF beam launched from the LFS passes through the vessel and reflects from

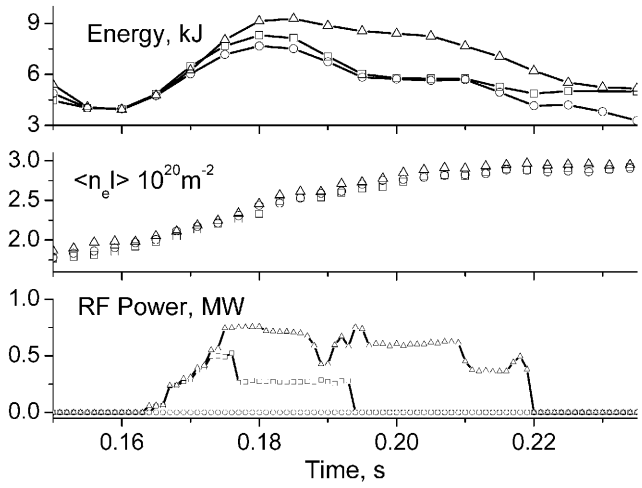

Fig. 16. Plasma energy increase in ohmic H-mode plasma during RF injection. Shots #10704, #10707, and #10709.

the grooved mirror-polarizer incorporated into the graphite tile on the central rod. The polarization of the reflected beam is converted into the X-mode polarization. As a result the reflected beam becomes completely trapped within the UHR surface (initially almost coincident with the fundamental EC resonance surface) as soon as RF preionization produces initial electron density.

2. Second, the X-mode produces intensive ionization near the UHR (close to 100% absorption) and quickly builds up electron pressure. In the presence of a TF and a weak vertical field, an electron drift should generate pressure-driven currents, which form an "open field equilibrium." Because of a "spontaneous current jump" mechanism,[46] a tokamak-like equilibrium with closed flux surfaces can then be formed.

3. Third, as initial equilibrium is achieved and electron temperature exceeds 10 to 20 eV, collisional absorption at UHR is weakened and cyclotron absorption becomes predominant. From that moment, the X-mode is completely converted into the EBW-mode at the UHR, which propagates back to the EC resonance. EBWs are absorbed by electrons at the Doppler-shifted EC resonance and generated current should cause further improvement of plasma confinement.

These three intrinsic stages separately have been experimentally demonstrated on a number of tokamaks.[2,13,46–49] The proposed scenario combines their

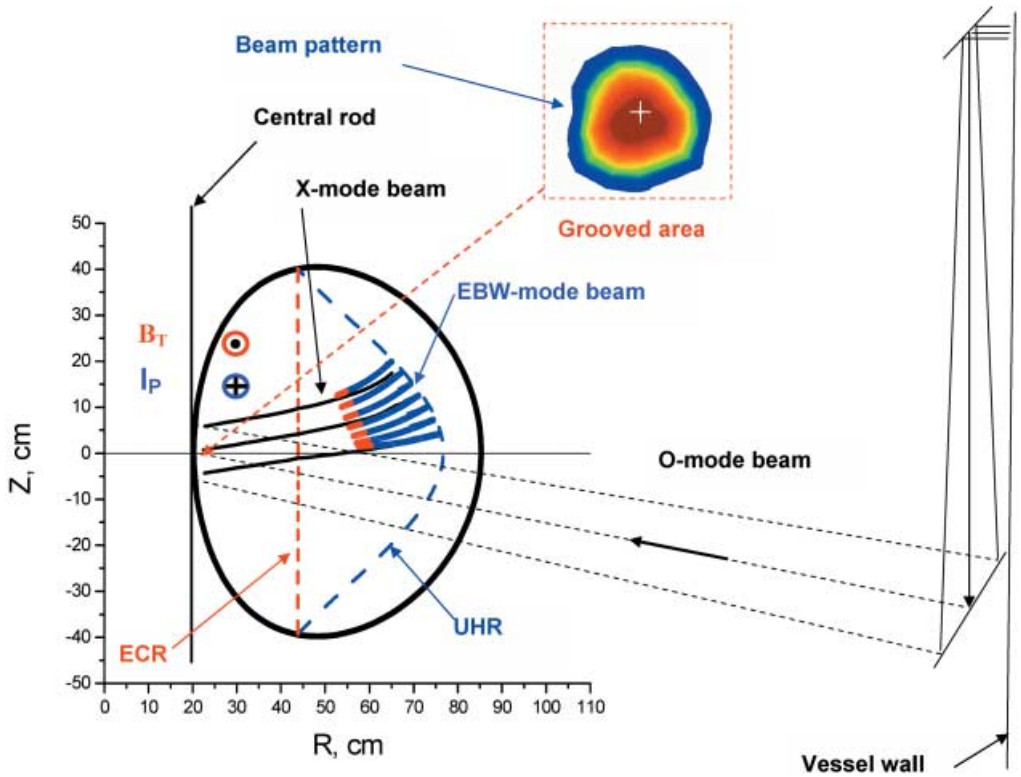

Fig. 17. Schematic (poloidal view) of the EBW CD plasma initiation. EBW ray-tracing simulations were performed with experimental data. The equilibrium was taken from a solenoid start-up scenario at 30 ms, shot #9867 in MAST. The RF beam pattern, as measured at low power, is well within the grooved area of the graphite mirror-polarizer.

advantages in order to achieve a substantial (~100 kA) noninductive plasma current in MAST. The plasma obtained with the proposed start-up scenario is restricted to low densities ($n_{e0} < 10^{19}$ m^{-3} for 28 GHz) to allow O-mode propagation to the mirror-polarizer. As soon as the start-up phase is completed, the plasma current, in principle, can be sustained further by EBW CD based on O-X-B MC of the lower-frequency wave launched from the LFS. The only requirement for such continuation is a high enough density for the second frequency ($n_{e0} > 4 \times 10^{18}$ m^{-3} for 18 GHz). No limitations on the further density increase are applied.

The 28-GHz start-up system has been designed and is now being commissioned in MAST. The gyrotron is capable of delivering up to 200 kW for 40 ms. The transmission line configuration is identical to the 60-GHz transmission lines. Smooth circular waveguides 40 mm in diameter are employed for the TE_{01} mode, and corrugated waveguides 45 mm in diameter are used for the HE_{11} mode at the machine end of the transmission line. The entrance into the vacuum vessel and final focusing of the RF beam is done quasi-optically. The launcher consists of two ex-vessel and three in-vessel ellipsoidal mirrors. The last launching mirror is located ~30 cm below the midplane. It reflects the RF beam toward the midplane at the central rod where the mirror-polarizer is machined on the surface of the graphite tile (see Fig. 17). Low-power tests have been conducted using a full-scale mock-up assembly of the launcher before installation in MAST. The RF beam pattern measured at the graphite tile shows that the beam is very close to Gaussian and 98% of the power is well within the grooved area of the mirror-polarizer. The 28-GHz system will be installed in MAST by the end of 2006.

VIII. CONCLUSIONS

A dedicated complex of high-power RF heating systems, EBW diagnostics, and modeling tools has been developed at Culham in order to assess the potential of EBW heating and CD for future applications in STs. The complex includes the ~1-MW, 60-GHz RF heating system equipped with the seven-beam steerable launcher, the 0.2-MW, 28-GHz plasma current start-up system, the panoramic frequency-scanning EBW radiometer, the RF mode matching heterodyne radiometer, LH probe with spectrum analyzer, and the integrated EBW modeling package.

Proof-of-principle EBW heating experiments have been conducted in MAST using three special plasma scenarios. It was shown that the O-X-B mode-coupling efficiency was no less than 50% in high-density ELM-free H-mode plasmas. In sawtoothing H-mode plasmas, a 10% increase of plasma energy was measured during RF injection. In small ohmic H-mode plasmas the enhanced SXR emission and ~10% increase of electron temperature were measured. EBW heating has therefore clearly been observed in MAST via the O-X-B MC process.

ACKNOWLEDGMENTS

This work has been funded jointly by the United Kingdom Engineering and Physical Sciences Research Council and by the European Communities under the contract of association between EURATOM and UKAEA. The views and opinions expressed in this paper do not necessarily reflect those of the European Commission.

REFERENCES

1. A. G. LITVAK et al., *Phys. Lett. A*, **188**, 64 (1994).

2. V. SHEVCHENKO et al., *Phys. Rev. Lett.*, **89**, 265005 (2002).

3. H. P. LAQUA et al., *Phys. Rev. Lett.*, **90**, *7*, 075003 (2003).

4. O. SAUTER et al., *Phys. Rev. Lett.*, **84**, *15*, 3322 (2000).

5. R. PRATER, *Phys. Plasmas*, **11**, *5*, 2349 (2004).

6. A. D. PILIYA and A. POPOV, *Plasma Phys. Control. Fusion*, **44**, 467 (2002).

7. A. BERS and A. K. RAM, *Phys. Lett.*, **A308**, 442 (2002).

8. V. SHEVCHENKO et al., *Proc. 13th Joint Workshop on Electron Cyclotron Emission and Electron Cyclotron Resonance Heating*, Nizhny Novgorod, Russia, May 17–20, 2004, p. 162, Institute of Applied Physics (2004).

9. G. TAYLOR et al., *Phys. Plasmas*, **11**, *10*, 4733 (2004).

10. V. SHEVCHENKO et al., *Proc. 13th Joint Workshop on Electron Cyclotron Emission and Electron Cyclotron Resonance Heating*, Nizhny Novgorod, Russia, May 17–20, 2004, p. 255, Institute of Applied Physics (2004).

11. V. E. GOLANT, *Phys. Scr.*, **T2/2**, 428 (1982).

12. V. PETRILLO et al., *Plasma Phys. Control. Fusion*, **29**, 877 (1987).

13. T. MAEKAWA et al., *Phys. Rev. Lett.*, **86**, 3783 (2001).

14. F. C. MCDERMOTT et al., *Phys. Fluids*, **25**, *9*, 1488 (1982).

15. J. PREINHAELTER and V. KOPECKY, *J. Plasma Phys.*, **10**, 1 (1973).

16. E. MJØLHUS, *J. Plasma Phys.*, **31**, 7 (1984).

17. A. P. PILIYA and E. N. TREGUBOVA, *Plasma Phys. Control. Fusion*, **47**, 143 (2005).

18. E. D. GOSPODCHIKOV et al., *Plasma Phys. Control. Fusion*, **48**, 869 (2006).

19. A. POPOV et al., *Plasma Phys. Reports*, **33**, 109 (2007).

20. V. L. GINZBURG, *Propagation of Electromagnetic Waves in Plasmas*, Nauka, Moscow (1967); Pergamon, Oxford (1970).

21. V. E. GOLANT and A. D. PILIYA, *Sov. Phys.—Usp.*, **14**, *4*, 413 (1972).

22. A. BERS et al., *Proc. 2nd Europhysics Topl. Conf. Radio Frequency Heating and Current Drive of Fusion Devices*, Brussels, Belgium, January 20–23, 1998, p. 237, European Physical Society (1998).

23. A. K. RAM et al., *Phys. Plasmas*, **7**, *10*, 4084 (2000).

24. A. K. RAM et al., *Phys. Plasmas*, **9**, *2*, 409 (2002).

25. B. JONES et al., *Phys. Rev. Lett.*, **90**, *16*, 165001 (2003).

26. H. P. LAQUA et al., *Phys. Rev. Lett.*, **78**, *18*, 3467 (1997).

27. R. A. CAIRNS et al., *Phys. Plasmas*, **7**, *10*, 4126 (2000).

28. V. SHEVCHENKO, *Plasma Phys. Reports*, **26**, 1000 (2000).

29. A. D. PILIYA and V. I. FEDOROV, *Sov. Phys.—JETP*, **30**, *4*, 653 (1970).

30. F. R. HANSEN et al., *J. Plasma Phys.*, **39**, *2*, 319 (1988).

31. V. PETRILLO et al., *J. Phys. Soc. Jpn.*, **58**, *7*, 2402 (1989).

32. M. A. IRZAK et al., *Plasma Phys. Reports*, **25**, 601 (1999).

33. M. A. IRZAK et al., *Plasma Phys. Reports*, **27**, 141 (2001).

34. J. PREINHAELTER et al., *Europhysics Conference Abstracts: 28th Conf. Controlled Fusion and Plasma Physics*, Funchal, Madeira, Portugal, June 18–22, 2001, Vol. 25A, p. 329, European Physical Society (2001).

35. H. IGAMI et al., *Plasma Phys. Control. Fusion*, **46**, 261 (2004).

36. V. SHEVCHENKO et al., *Proc. 15th Topl. Conf. Radio Frequency Power in Plasmas*, Moran, Wyoming, May 19–21, 2003, C. FOREST, Ed., p. 359, American Institute of Physics (2003).

37. J. PREINHAELTER et al., *Rev. Sci. Instrum.*, **75**, *10*, 3804 (2004).

38. D. CHENNA REDDY and T. EDLINGTON, *Rev. Sci. Instrum.*, **67**, *2*, 462 (1996).

39. V. SHEVCHENKO et al., *Europhysics Conference Abstracts: 27th Conf. Controlled Fusion and Plasma Physics*, Budapest, Hungary, June 12–16, 2000, Vol. 24B, p. 3.120, European Physical Society (2000).

40. B. JONES et al., *Phys. Plasmas*, **11**, *3*, 1028 (2004).

41. M. WALSH et al., *Rev. Sci. Instrum.*, **74**, *3*, 1663 (2003).

42. A. N. SAVELIEV, *Plasma Phys. Control. Fusion*, **47**, 2003 (2005).

43. M. O'BRIEN et al., *Proc. Technical Committee Mtg. Advances in Simulation and Modelling of Thermonuclear Plasmas*, Montreal, Quebec, Canada, June 15–17, 1992, p. 527, International Atomic Energy Agency (1993).

44. V. SHEVCHENKO et al., *Proc. 14th Joint Workshop on Electron Cyclotron Emission and Electron Cyclotron Resonance Heating*, Santorini Island, Greece, May 9–12, 2006, p. 54, A. LAZAROS, Ed., Heliotopos Conferences, Ltd. (2006).

45. A. SURKOV et al., *Europhysics Conference Abstracts: 32nd Conf. Plasma Physics and Controlled Fusion*, Tarragona, Spain, June 27–July 1, 2005, Vol. 29C, p. 5.103, European Physical Society (2005).

46. T. YOSHINAGA et al., *Phys. Rev. Lett.*, **96**, 125005 (2006).

47. M. GRYAZNEVICH et al., *Nucl. Fusion*, **46**, S573 (2006).

48. C. B. FOREST et al., *Phys. Plasmas*, **1**, *5*, 1568 (1994).

49. T. MAEKAWA et al., *Nucl. Fusion*, **45**, 1439 (2005).